***In vitro* cytocompatibility of a Zr-based metallic glass modified by laser surface texturing for potential implant applications**

Yang Jiao[1], Emmanuel Brousseau[1*], Wayne Nishio Ayre[2], Edward Gait-Carr[2], Xiaojun Shen[3], Xiaoxiang Wang[4], Samuel Bigot[1], Hanxing Zhu[1], Weifeng He[5]

1. Cardiff School of Engineering, Cardiff University, Cardiff, CF24 3AA, United Kingdom

2. Department of Oral and Biomedical Sciences, School of Dentistry, Cardiff University, Cardiff, CF14 4XY, United Kingdom

3. School of Mechanical, Aerospace and Automotive Engineering, Coventry University, Coventry, CV1 5FB, United Kingdom

4. Institute of Industrial Ecology and Environment, College of Chemical and Biological Engineering, Zhejiang University, Hangzhou, 310027, China

5. Institute of Aeronautics Engine, School of Mechanical Engineering, Xi'an Jiaotong University, Xi'an, Shaanxi, 710049, China

Abstract: Existing studies have shown the benefit of laser surface texturing (LST) in promoting the cytocompatibility of traditional metallic biomaterials. Researchers have also reported the potential of bulk metallic glasses (BMGs) as an alternative class of material for biomedical applications. However, investigations specifically focussed on studying the cytocompatibility of BMG surfaces processed with LST are still lacking. The present work demonstrated the feasibility of nanosecond LST as a method to modify the cytocompatibility of a Zr-based BMG material known as Vitreloy 105. Two different types of laser-induced surface patterns, namely grooves and dimples, were considered. Their respective influence on the resulting cell viability, attachment and morphology was studied and compared against the cytocompatibility of the original BMG surface. It was found that MG63 osteoblast-like cells on the groove-textured surface exhibited higher viability and better adhesion compared to those on the original and dimple-textured surfaces. Possible underlying mechanisms associated with LST, which can affect the *in vitro* cytocompatibility of Vitreloy 105 were discussed based on the induced changes to surface chemistry, wettability and roughness. It is suggested that the higher surface roughness, increased presence of metallic oxides and enhanced hydrophilicity of the groove-textured sample were the main contributors to its improved cytocompatibility.

1. Introduction

The consideration of bulk metallic glasses (BMGs) for biomedical applications has drawn growing interest from the scientific community in recent years [1]. This is due to the remarkable mechanical and chemical properties of BMGs, which include low elastic modulus [2], high wear resistance [3], good corrosion resistance [4], and favourable processing capabilities [5].

These valuable engineering attributes results from their unique atomic structure, characterised by a lack of long-range order leading to the absence of crystal defects and grain boundaries [6]. In comparison with traditional biomedical alloys, i.e. titanium alloys, stainless steels and magnesium alloys, the interesting properties of BMGs have promoted the gradual consideration of such glassy alloys as potential candidate biomaterials, especially for implants and surgical tools [7]. It was noted that such favourable mechanical properties could be particularly beneficial in reducing the occurrence of some of the current medical complications associated with traditional biomedical alloys used for implant applications, such as stress shielding, wear particle induced inflammation, corrosion–fatigue failure and foreign body inflammation [8]. Moreover, the unique thermo-plastic deformation behaviour of BMGs in their supercooled liquid region and their small solidification shrinkage could enable the fabrication of net-shape complex medical devices, hence reducing the number of processing operations [9].

However, when considering any candidate biomaterial, a thorough cytocompatibility assessment, including *in vitro* cellular response and *in vivo* tissue response, must be conducted. A number of studies exploring the cytocompatibility of BMGs has already been carried out, the outcome of which has generally shown the potential of Zr-based, Mg-based and Ti-based BMGs for biomedical applications [1, 2, 8, 10]. For example, among these different types of BMGs, it was reported that a Zr-based composition, which also included the elements Cu, Fe, Al and Ag, was suitable for application as long-term implants due to observed favourable mechanical properties, good glass forming ability and excellent cytocompatibility [10]. In addition, surface treatments such as coatings [11], ion implantation [12] and laser surface texturing (LST) [13], have been successfully employed on traditional biomedical alloys, especially titanium alloys, to further enhance their cytocompatibility. Among these methods, LST has been considered as a promising technique for modifying the surface properties of biomaterials due to being flexible, simple, and displaying good controllability and reproducibility [14]. In fact, numerous investigations have now been reported that focussed on investigating the cytocompatibility of traditional biomedical alloys treated by LST [13, 15-19]. In the case of femtosecond laser processing on a titanium substrate, LST has been shown to avoid the introduction of toxic substances on the irradiated metallic surface [20]. In addition, Kumari et al. [13] found that laser texturing a Ti-6Al-4V surface resulted in a comparable cell viability to that of the as-received titanium alloy surface. Hsiao et al. [15] used an ultraviolet laser to produce micro-grooves on a Ti-6Al-4V workpiece and compared the osteogenic cell growth between the as-received and laser-textured surface. These authors observed that the laser-induced groove texture could provide a favourable environment for osteogenic cells to

proliferate. Femtosecond laser processing was also successfully exploited by Lee et al. [16] to generate sub-micrometre patterns, which improved cell viability on a titanium substrate. Mukherjee et al. [17] reported that laser-induced surface features, which were dimensionally close to the size of the cells, could positively affect cell viability and migration on Ti6Al4V. Moreover, Ohtsu et al. [18] improved the cellular adhesiveness and cell proliferation by laser texturing on titanium. Zhou et al. [19] investigated the effect of picosecond laser texturing on the cytocompatibility of a titanium alloy, and concluded that the fabricated micro-grooves helped cell adhesion, cell growth and contact guidance. These authors also observed that increased groove depth could lead to more obvious cell contact guidance. Overall, this body of literature suggests the benefits of LST in promoting the cytocompatibility of traditional metallic biomaterials. However, in the context of BMGs, research investigations are still required to study the cytocompatibility of such surfaces specifically post-LST. In particular, it is of interest to find out whether LST can also be used on purpose to modify cell viability and attachment when considering a BMG surface. In addition, it is relevant to observe whether texturing the groove pattern can also lead to the most favourable cytocompatibility as tends to be the case on titanium alloys. Finally, there is scope to try to understand possible underlying mechanisms associated with changes in cytocompatibility when preparing BMG surfaces with LST.

The objective of the research reported here was to address this knowledge gap when processing a Zr-based BMG with a nanosecond laser. When conducting this investigation, the objective was also to explore associated underlying physical phenomena that take place as a result of laser texturing the considered BMG substrate. To achieve this goal, the specific $Zr_{52.8}Cu_{17.6}Ni_{14.8}Al_{9.9}Ti_{4.9}$ (at%) BMG, also known as Vitreloy 105, was considered. The selection of this particular glassy alloy was motivated by the fact that it does not contain the toxic element beryllium, in comparison with the better known Vitreloy 1 composition, and that it exhibits excellent fatigue characteristics among most BMGs [21]. In addition, based on the body of studies for which LST was applied on traditional biomedical alloys, it was decided to investigate patterns generated in the shape of grooves and dimples on the surface of Vitreloy 105 specimens. The surface topography, chemical composition and surface wettability of the processed surfaces was assessed via non-contact three-dimensional confocal microscopy, scanning electron microscopy, X-ray photoelectron spectroscopy and contact angle measurements. The viability, attachment and morphology of MG63 osteoblast-like cells was evaluated on different textured surfaces using a tetrazolium-based viability assay and fluorescent staining of actin filaments, a major component of the cell cytoskeleton. Finally, an attempt was made to discuss the relationship between the modified cytocompatibility and the

combined influence of surface chemical composition, roughness and wettability changes resulting from the laser texturing of the Zr-based BMG. It is anticipated that the results of this work can provide some guidance when considering selection of the Vitreloy 105 BMG composition for implants applications.

2. Experimental procedures

2.1 Sample preparation

As mentioned earlier, the Zr-based metallic glass with nominal composition $Zr_{52.8}Cu_{17.6}Ni_{14.8}Al_{9.9}Ti_{4.9}$ (at%) was used in this study. Specimens were purchased from the company Visser Precision (Denver, USA). During the fabrication process, the molten alloy with the above composition was cast into a mould using vacuum injection moulding to produce cylindrical rods with a diameter of 3 mm and a length of 10 mm. Upon delivery from this supplier, the rods were cut into smaller disk specimens with a length of 3 mm using micro-wire electrical discharge machining. These cylindrical rods (i.e. 3 mm in diameter and 3 mm in length) were then manually ground using coarse abrasive paper (180 grit) and subsequently polished with 1200 and 2000 grit SiC papers, followed by a final step using a 1 μm diamond gel suspension until a mirror-like appearance was obtained. All specimens were mounted in conductive resin prior to polishing to facilitate handling and mounting in the polishing machine and in any microscopy equipment subsequently required. After polishing, all samples were cleaned in an ultrasonic bath using acetone and distilled water for 15 minutes. Before conducting the biochemical tests, the samples were sterilized in an autoclave for approximately 15 minutes at 121 °C and 1.4 bar.

Fig. 1(a) displays the XRD pattern of the as-cast Vitreloy 105 material. This figure shows that the metallic glass matrix presents an overall broad halo. However, two crystalline peaks are also visible, suggesting that the BMG specimens were not fully amorphous. Fig. 1(b) shows data from a DSC scan of the alloy at a heating rate of 0.04 K/s. The onsets of the glass transition temperature (T_g), crystallization temperature (T_{x1}) and melting temperature (T_m) were measured to be 687 K, 721 K and 1093 K, respectively. These values are in reasonable agreement with those measured by Glade et al. [22], who conducted a thermodynamic study of a very similar alloy composition, i.e. $Zr_{52.5}Cu_{17.9}Ni_{14.6}Al_{10}Ti_5$, shortly after it was first reported by Lin et al. [23] in 1997. The supercooled liquid region, ΔT, which is assessed between T_{x1} and T_g was estimated to be 34 K. This indicates that the Vitreloy 105 material had a relatively good glass forming ability.

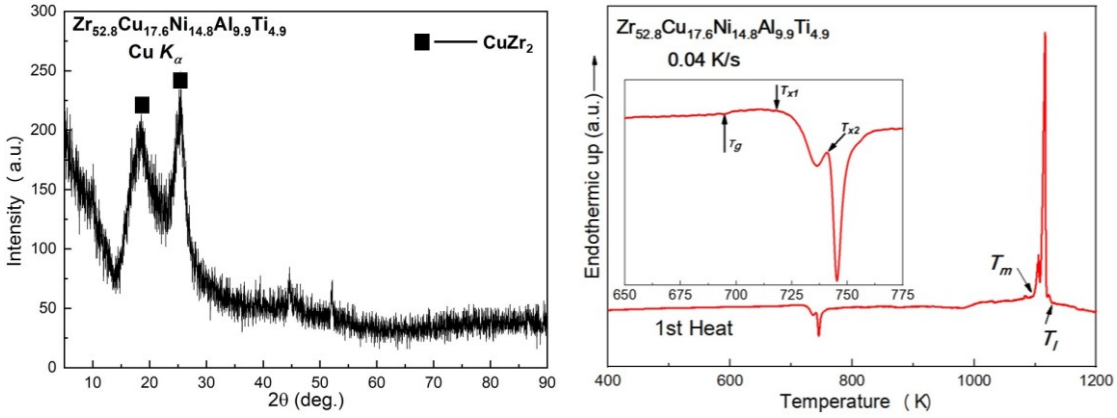

(a) (b)

Fig. 1. (a) XRD pattern and (b) DSC curve of the as-cast Vitreloy 105 material.

Two types of surface textures, dimples and grooves, were machined on the Zr-based metallic glass surface using a nanosecond fibre laser from SPI Lasers (Southampton, United Kingdom). This laser displayed a wavelength of 1024 nm and was operated with a pulse duration of 220 ns and a pulse repetition frequency of 20 kHz. In this system, the laser source was stationary, and the processed specimen fixed on a high-resolution computer controlled 3-axis motion platform to achieve the required patterning path. All surface textures were machined under the same laser fluence of 30 J/cm^2, and also with the same "distance" of 90 µm. More specifically, the parameter "distance" for the dimple-textured surface was the distance between two adjacent single craters, while for the groove-textured surface, this was the distance between two adjacent linear grooves. In addition, the scanning speed for the groove-textured samples was fixed at 200 mm/s, which resulted in a pulse overlap of 68.8 %. The laser parameters used for the LST experiments are summarised in Table 1.

Table 1 Laser parameters for the fabrication of dimple and groove patterns on the surface of the Vitreloy 105 samples.

Wavelength (nm)	Spot diameter (µm)	Pulse duration (ns)	Frequency (kHz)	Laser fluence (J/cm^2)	Track distance (µm)	Scanning speed (mm/s)	Surface patterns
1064	32	220	20	30	90	-	Dimples
						200	Grooves

2.2 BMG surface characterization

The chemical composition of the Zr-based BMG surfaces before and after laser processing was investigated using a Thermo-Scientific ESCALAB^{TM} Xi$^+$ X-ray photoelectron spectrometer (XPS; Thermo-Scientific, USA). The monochromatic Al Kα X-ray source was used for the

measurement and XPS PEAK4.1 software was employed to analyse the data. Both the survey and narrow scan spectra were recorded from an analysed area 300 × 700 μm^2 on each BMG sample. The surface roughness of all the specimens was measured using a non-contact three-dimensional surface profiler (S mart Series, Sensofar Co., Barcelona, Spain) with the associated analysis software (SensoMap, Sensofar Co.). Each specimen was observed at x20 magnification, which corresponded to a visible area of 850 × 710 μm^2. Qualitative surface morphology information was obtained using a field-emission scanning electron microscope (FE-SEM; 1540XB from Carl Zeiss, Germany) using its secondary electron detector. The surface wettability was characterized by the sessile drop contact angle method using distilled-deionized water (DD water) and ethylene glycol (EG) and a DataPhysics OCA100 contact angle goniometer (DataPhysics Co., Germany). The surface free energy (SFE) of all the samples was calculated based on the contact angle measurements using the Owens–Wendt equation [24].

$$1 + cos\,\theta = 2(\gamma_S^d)^{1/2}\left[(\gamma_L^d)^{1/2}/\gamma_L\right] + 2\left(\gamma_S^p\right)^{1/2}\left[\left(\gamma_L^p\right)^{1/2}/\gamma_L\right] \quad (1)$$

where θ is the contact angle, γ_L is the SFE of the liquid used in the measurement, γ_S is the SFE of the test sample and the superscripts d and p denote the dispersive and polar components of SFE. The surface free energy of two testing liquids used in this study, as well as their dispersive and polar components are given in Table 2. The total surface free energy, γ_S^T, of the test sample is the sum of the polar components γ_S^p and the dispersive components γ_S^d .

Table 2 Surface free energy characteristics of the liquids employed for surface wettability tests.

Liquid	Dispersive energy (γ_L^d) (mN/m)	Polar energy (γ_L^p) (mN/m)	Total surface energy (γ_L^T) (mN/m)
Distilled-deionized water	21.8	51	72.8
Ethylene glycol	29	19	48

2.3 Cell culture and viability

The human MG63 osteoblast-like cell line was used in this study. Cells (passages 28-32) were maintained in T75 cell culture flasks in culture medium, comprising of alpha minimum essential medium (α-MEM) supplemented with 10% (v/v) heat-inactivated fetal bovine serum (FBS), 100 units/mL penicillin G sodium, 0.1 μg/mL streptomycin sulfate, and 0.25 μg/mL amphotericin. The cells were incubated at 37°C, 5% CO_2 with the medium changed every 2-3 days. Cells were cultured until approximately 80-90% confluent before being used for subsequent experiments.

Cellular responses, i.e. cell viability, attachment and morphology, are considered to be good indicators to evaluate the cytocompatibility of a potential biomaterial [25]. In this study, the cell counting Kit-8 (CCK-8) assay (Sigma-Aldrich, USA) was used to investigate the cell viability due to its high detection sensitivity. This assay is based on the cellular conversion of a tetrazolium salt into a soluble formazan dye, which can be characterized by optical density measurements. The amount of formazan dye generated by the activity of dehydrogenases in the cells is directly proportional to the number of living cells [26, 27]. The cells were seeded directly on the as-cast (AC), laser dimple-textured (DT) and laser groove-textured (GT) BMG specimens in 96-well plates at a density of 15,000 cells/cm^2 (approximately 1500 cells per sample) and incubated for 1h at 37°C, 5% CO_2 to allow attachment. The wells were then flooded with supplemented culture media and incubated for a further 24 hours. Subsequently, the specimens with seeded cells were washed three times with phosphate buffered saline (PBS) to remove non-adherent cells, and then transferred to fresh 96-well plates with 100 µL media in each well. 10 µL of the CCK-8 reagent was added to each well and incubated for 3 hours according to the manufacturer's instructions. Finally, colorimetric measurement of the formazan dye was performed on a microplate reader with an optical density reading at 450 nm. An empty well with no cells was used as the negative control and a well with 1500 cells was used as a positive control. The experiment was repeated in triplicate (n=3) and the average OD value was taken as the final result for each group. Further, the student *t*-test statistical procedure was applied on all possible combination of pairs between AC, GT and DT surfaces where a *p*-value less than 0.05 was considered statistically significant.

2.4 Cell attachment and morphology

Following the absorbance measurements, the medium was replaced with 10% formalin to fix the attached cells, which were then incubated at 4°C overnight. Following incubation, the 10% formalin solution was removed, and the cells were washed three times with tris-buffered saline (TBS). The cells were permeabilised with filtered 1% Triton X-100 (Sigma-Aldrich) for 30 minutes at room temperature (RT) and washed three times with TBS, followed by blocking with 1% normal horse serum (Vector Laboratories, UK) in TBS for 1 hour at RT. The actin filament of the cells were stained with freshly prepared phalloidin reagent (phalloidin fluorescein isothiocyanate labelled, Sigma-Aldrich) at a ratio of 1:50 in TBS and left for 40 mins at RT. Cells were washed 3 times with TBS and left for 5 mins to dry. 10 µL of DAPI (Vectashield Hard Set, Vector Laboratories, UK) was added to each sample surface to stain the nuclei of the cells. Cell attachment and morphology analysis was performed on the fluorescent images obtained via an AX70 Olympus Provis fluorescent microscope.

3. Results

3.1 Surface characterization

Fig. 2 shows the surface topography of the BMG samples, without (i.e. as-cast: AC) and with (i.e. dimple-textured: DT and groove-textured: GT) surface texturing, observed with the 3D optical microscope and field-emission scanning electron microscope. The DT surface was generated by creating an array of single craters, with each crater corresponding to a single pulse irradiation event. On this surface, rims and vapour particles were distributed around the craters as a result of the laser-material interaction phenomena, as discussed in a former laser-based study on this specific type of substrate material [28]. Grooves and ridges could also be observed clearly on the GT samples, while naturally, no surface features were visible on the as-cast (i.e. AC) samples. The measured dimensions (i.e. depth, diameter or width) and surface roughness values of these three types of surfaces are listed in Table 3 using the arithmetical average height of the specific surface area, S_a. For the AC sample, S_a was assessed to be 0.065 μm, while for the DT and GT samples the measured S_a increased to 0.21 μm and 3.24 μm, respectively. The average depths of a single crater for the DT specimen and of a groove for the GT surface were 2.44 μm and 10.2 μm, respectively. In addition, their corresponding diameter and width were 32.2 μm and 28.6 μm, respectively. It was reported in the literature that increased surface roughness is beneficial for cell attachment and cell orientation on titanium alloys [29]. The effects of the two types of surface textures considered here on the cell behaviour for the Zr-based metallic glass from the perspective of surface roughness variation is discussed more specifically in section 4.

Fig. 3 shows the XPS spectra of the metallic glass specimens for all three types of surfaces. For the AC sample, primary peaks were identified as Zr 3*d*, Cu 2*p*, Ni 2*p*, Al 2*p*, Ti 2*p*, C 1*s* and O 1*s*, as shown in Fig. 3(a). The detected C 1*s* and O 1*s* peaks in the spectrum may result from the contamination and oxidation on the sample surface. After laser irradiation, all peaks for Zr 3*d*, Cu 2*p*, Ni 2*p*, Al 2*p*, Ti 2*p*, C 1*s* and O 1*s* could still be detected on the DT and GT surfaces. This shows that laser irradiation did not lead to the disappearance of any chemical elements. However, the specific quantitative composition may still have changed. Accurate chemical compositions were calculated from the XPS spectra and these are summarized in Table 4. It can be seen from this table that carbon content was increased from 58.89 % for the AC sample to 72.87% for the DT sample and to 75.46% for the GT specimen. This increase could be ascribed to the formation of hydrocarbons induced during LST. However, the oxygen and zirconium contents both decreased. More specifically, the oxygen content was reduced from 28.58% (AC) to 18.23% (DT) and 17.12% (GT). This indicates that the laser irradiation

may have contributed to remove the oxide layer on the as-cast sample surface. The zirconium content was decreased from 4.77% (AC) to 1.33% (DT) and to 1.08% (GT). In addition, the other elements, i.e. copper, nickel, aluminium and titanium, always displayed a low concentration for all samples due to contamination on the surface with carbon and oxygen. These elements only underwent slight change after laser texturing, as evidenced in Table 4. Since the relative contributions of nickel and copper for all samples are very low, their narrow spectra analysis is not shown in the follow-up analysis.

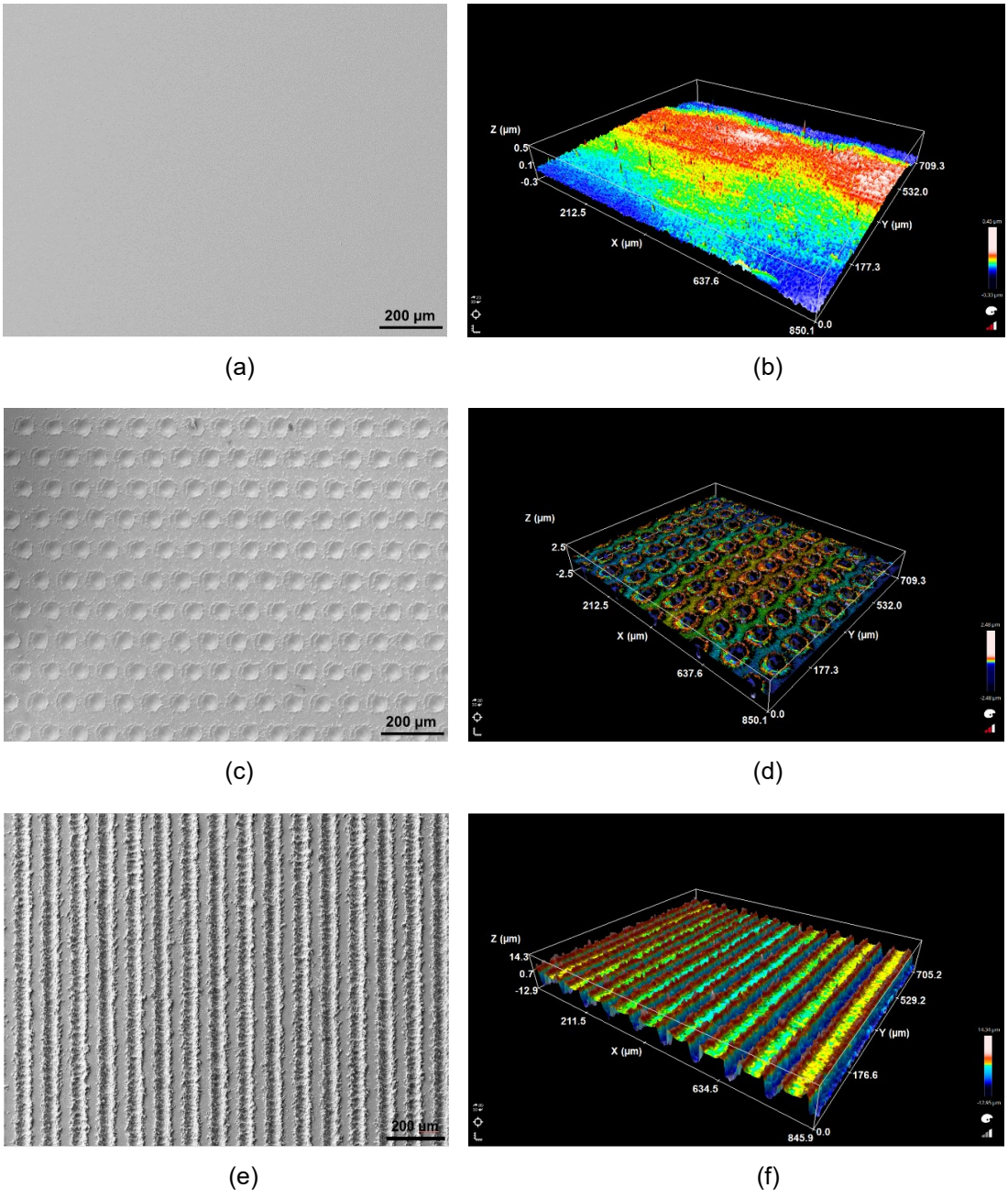

Fig. 2. SEM images of Vitreloy 105 surfaces (a, c, e) and their corresponding 3D topography (b, d, f). (a)(b) for the as-cast, (c)(d) for the dimple textured and (e)(f) for the groove textured sample.

Table 3 Dimensional and roughness data for different samples.

Samples	Roughness S_a (μm)	Depth (μm)	Diameter (DT) or Width (GT) (μm)
Dimple textured (DT)	0.21 ± 0.06	2.44 ± 0.41	32.23 ± 2.16
Groove textured (GT)	3.24 ± 0.08	10.2 ± 0.21	28.6 ± 3.79
As-cast (AC)	0.065 ± 0.01	-	-

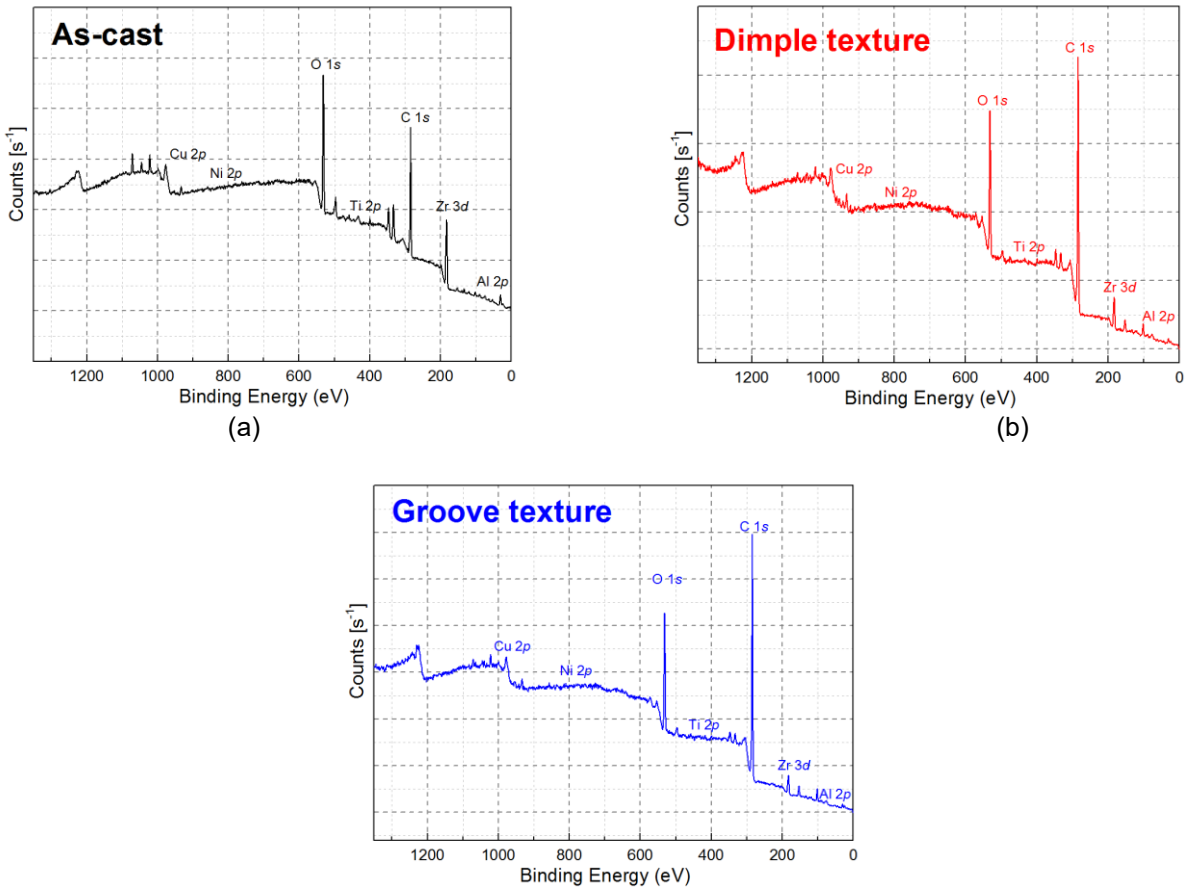

Fig. 3. XPS spectra of the Vitreloy 105 surface for the as-cast (a), dimple-textured (b) and groove-textured (c) specimens.

Table 4 Relative surface chemical compositions of Vitreloy 105 for the as-cast, dimple-textured and groove-textured specimens measured by XPS.

Samples	C (at. %)	O (at. %)	Zr (at. %)	Cu (at. %)	Ni (at. %)	Al (at. %)	Ti (at. %)
AC	58.89	28.58	4.77	0.76	0.44	5.69	0.87
DT	72.87	18.23	1.33	0.83	0.36	5.69	0.70
GT	75.46	17.12	1.08	0.73	0.38	4.58	0.66

High-resolution spectra from the AC, DT and GT samples are shown in Fig. 4 for the Zr 3*d*, Al 2*p*, Ti 2*p* and O 1*s* elements. Zirconium oxides (ZrO_2 and ZrO_x) and metallic Zr (i.e. pure Zr) were detected on the AC surface. In contrast, no trace of metallic Zr was observed on the surface of the samples after laser treatment, indicating that the zirconium on the surface was oxidized during LST. In the case of Ti 2*p*, all the samples showed a similar behaviour where the spectra revealed peaks at 458.5 eV and 464.2 eV corresponding to titanium oxide (TiO_2) doublets, Ti $2p_{1/2}$ and Ti $2p_{3/2}$, respectively. Moreover, for the Al 2*p* region, the XPS spectrum for the samples with and without laser texturing all show peaks at 72.6 eV, 74.6 eV and 76.8 eV corresponding to the metallic Al, Al_2O_3 and AlO(OH), respectively. After laser texturing the groove pattern, the data suggests a reduced content of the aluminium element, particularly Al_2O_3. The formation of titanium oxides, zirconium oxides and aluminium oxides can also be verified by examining the O 1*s* spectra shown in Fig. 4 (j) to (l).

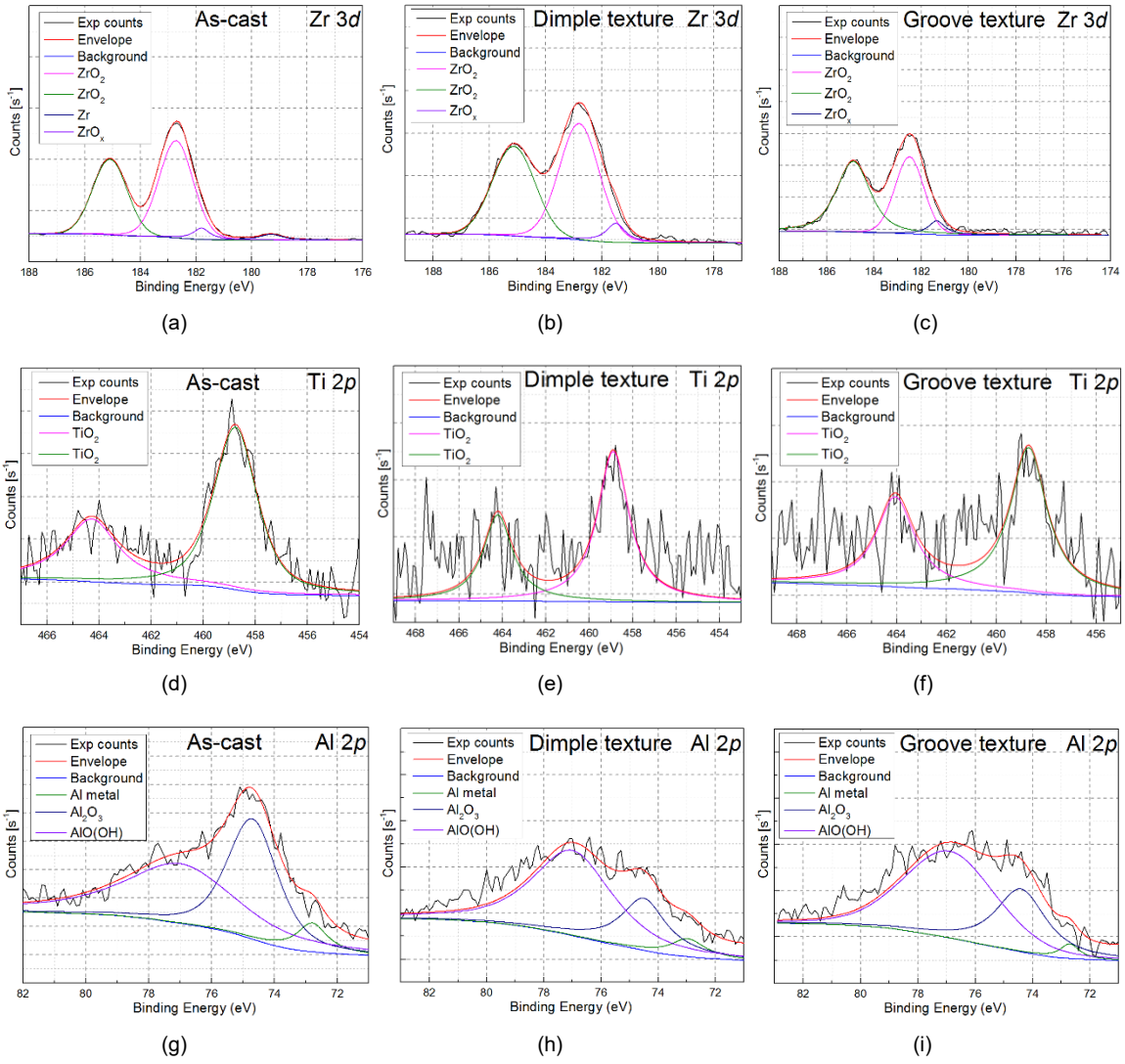

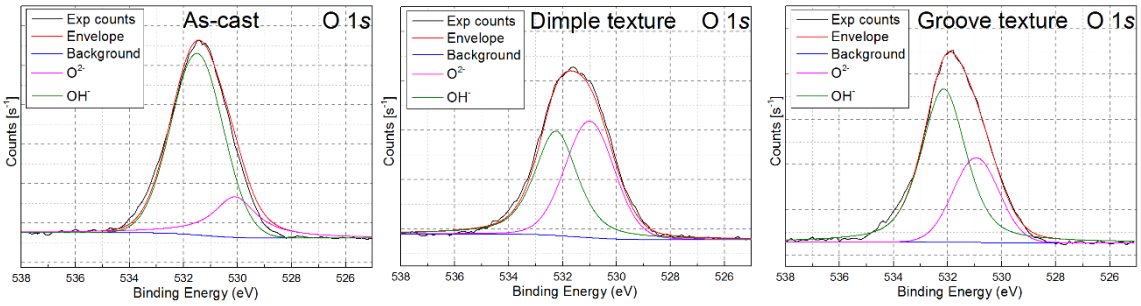

(j) (k) (l)

Fig. 4. High-resolution XPS spectra for the as-cast, dimple textured and groove textured samples: narrow scans of (a) to (c) for Zr 3*d*, (d) to (f) for Ti 2*p*, (g) to (i) for Al 2*p* and (j) to (l) for O 1*s*.

3.2 Wettability and SFE

Surface wettability in terms of static contact angle (SCA) was characterized by the sessile drop technique. The SCA value of the AC, GT and DT samples are presented in Fig. 5 and Table 5. Optical images of liquid droplets are also shown with the insets in Fig. 5. It should be noted that the SCA values on all samples were measured to be less than 65°, implying that all surfaces were found to be hydrophilic. However, the data reported in Fig. 5 shows that LST can induce an increase, as well as a decrease, of SCA values, depending on the type of texture generated. More specifically, the SCA of the DT sample was always higher than that of the AC sample for both types of liquid utilised. The opposite result was observed for the GT sample. This shows that the groove texture could enhance the hydrophilicity of the Vitreloy 105 surface, while the dimple texture could weaken it. The result for the GT pattern is consistent with the findings from Pfleging et al. [30] and Bizi-bandoki et al. [31], in which a laser-induced line texture was shown to enhance the hydrophilicity, albeit on other types of metallic alloys. With respect to the cytocompatibility of a surface, it has been reported in the literature that high hydrophilicity is beneficial for cell attachment and proliferation [32, 33].

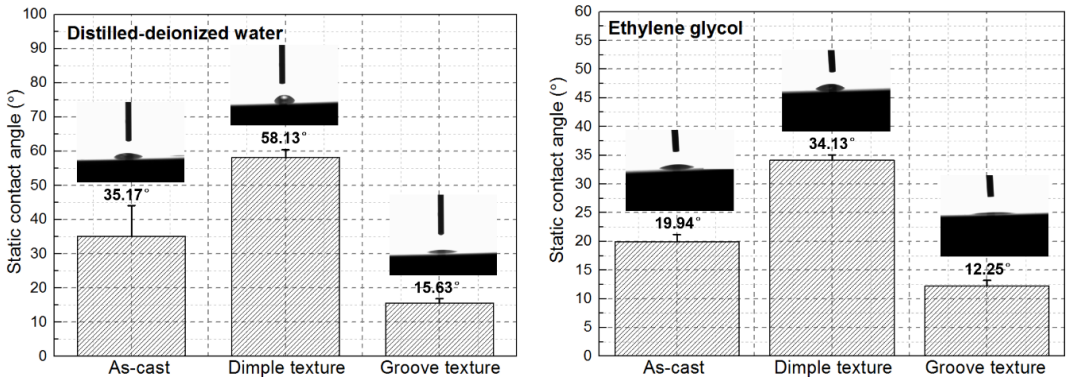

(a) (b)

Fig. 5. Static contact angles for the as-cast, dimple-textured and groove-textured surfaces wetted by distilled-deionized water (a) and ethylene glycol (b). The insets show optical images of the droplets.

Table 5 Static contact angle and surface free energy of as-cast and laser textured surface with groove and dimple textures.

Samples	Contact angle (°)		Surface free energy (mN/m)		
	DD water	Ethylene glycol	Dispersive (γ^d)	Polar (γ^p)	Total (γ^T)
As-cast	35.17	19.94	0.93	80.11	81.04
Dimple texture	58.13	34.13	12.78	29.83	42.65
Groove texture	15.63°	12.25°	0.38	118.92	119.3

The surface free energy (SFE) was calculated from the Owens–Wendt model based on the SCA values measured using the two liquids (i.e. distilled-deionized water and ethylene glycol). The SFE values for each specimen, along with the polar and dispersive components, are shown in Fig. 6, and also reported in Table 5. From Fig. 6, it should be noted that the SFE of the three types of surfaces were rather different. Indeed, the SFE value varied from 42.65 mN/m for the DT sample to 119.3 mN/m for the GT specimen, in comparison with 81.04 mN/m for the AC sample. Furthermore, the polar component of the SFE was significantly higher in the case of the GT surface (118.92 mN/m) compared to that of the AC (80.11 mN/m) and the DT (29.83 mN/m) surfaces. In contrast, the dispersive component of the SFE for the DT sample (12.78 mN/m) was much higher than that of the AC (0.93 mN/m) and the GT (0.38 mN/m) samples. The SFE of a material is reported to be determined by several characteristics, including surface chemical composition, surface topography and surface charge. However, the correlation between them is still not completely clear and needs to be explored further [13, 17, 34, 35]. The relationship between wettability, SFE and cellular behaviour for the different types of surface patterns considered on Vitreloy 105 is discussed in the subsequent sections.

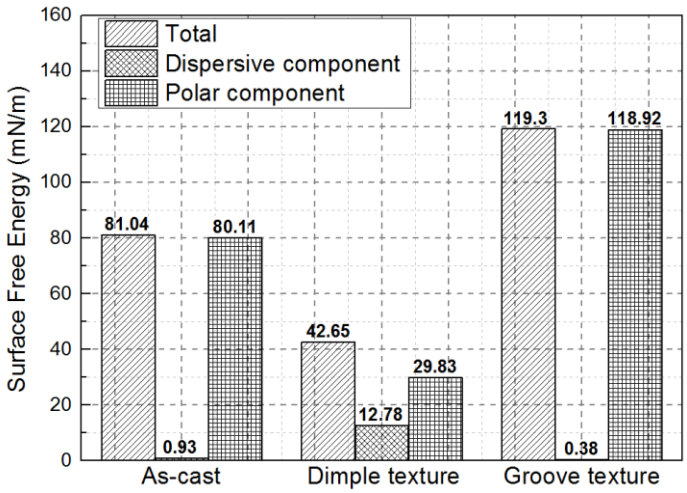

Fig. 6. Surface free energy, dispersive and polar components for the Vitreloy 105 BMG in the case of the as-cast surface as well as the dimple-textured and groove-textured surfaces.

3.3 Cell viability

Fig. 7 shows the cell viability characterized by the optical density (OD) of MG63 osteoblast-like cells on the AC, DT and GT surfaces as measured by the CCK-8 assay. It can be seen from this figure that the measured OD values for all three surfaces of interest were above the background OD value of the negative control (i.e. no cells). Moreover, they were comparable to, or larger than that of, the positive control sample (i.e. cells on tissue culture plastic). This means that the cells were able to survive on all three types of Vitreloy 105 surfaces and thus, that this BMG had no cytotoxic effect, whether as-cast or after the LST process. A detailed comparison of cell viability between the samples of interest showed that the OD values of the GT surface was the highest (0.66 ± 0.04, 122% relative to the positive control), and that of the AC surface (0.53 ± 0.03, 98% relative to the positive control) was slightly higher than that of the DT surface (0.52 ± 0.03, 96% relative to the positive control). Therefore, it can be concluded that the groove-textured surface led to greater cell viability, with a significantly higher viability compared to the AC surface (p<0.05). These cell viability results are in line with the wettability data reported earlier, and also with findings made by Mukherjee et al. [17] in the case of MG63 cells cultured on micro-groove patterns on the surface of a Ti-6Al-4V alloy.

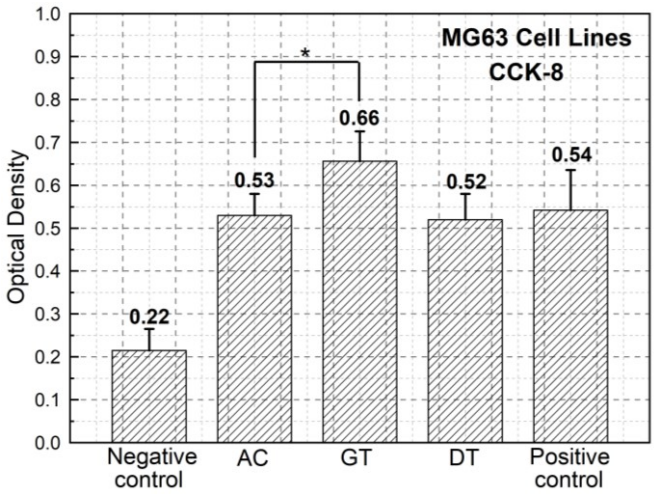

Fig. 7. Cell viability measured with CCK-8 assay of cells cultured on the Vitreloy 105 surface in the case of as-cast (AC), dimple-textured (DT) and groove-textured (GT) surfaces. The *t*-test was conducted on all possible combination of pairs between AC, GT and DT surfaces; the inclusion of the symbol * in this figure indicates that only the means between AC and GT were found to be significantly different from each other (p<0.05).

3.4 Cell attachment and morphology

Fig. 8 shows representative fluorescence microscopy images of the morphology of MG63 cells cultured for 24 h on the AC, DT and GT surfaces. Fig. 8(a) and (b) show the presence of cells attached to the as-cast Vitreloy 105 surface, stained by DAPI and phalloidin, respectively. In contrast, while almost no cells could be found on the dimple-textured surface (Fig. 8(c) and (d)), an increased amount could be seen on the groove-textured surface (Fig. 8(e) and (f)), which agrees with the cell viability results reported in the previous section. These observations confirmed that the laser-induced groove texture promoted cell attachment, whilst the dimple texture inhibited it. Merged fluorescent DAPI and phalloidin images for the AC and GT surfaces are also shown in Fig. 9. From this figure, it should be noted that the cells were randomly distributed on the as-cast Vitreloy 105 surface. However, the cells on the groove-textured surface tended to be aligned along the grooves, indicating preferential adherence, which is likely to impact on cell morphology and behaviour.

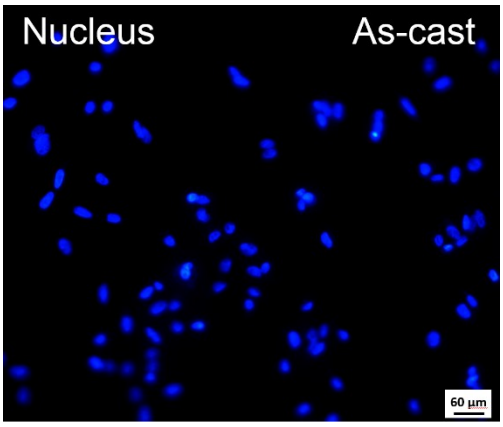

(a)

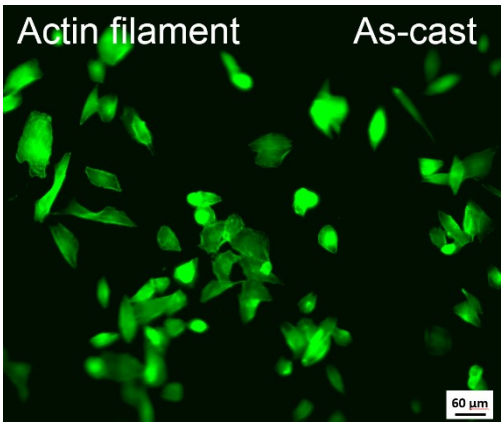

(b)

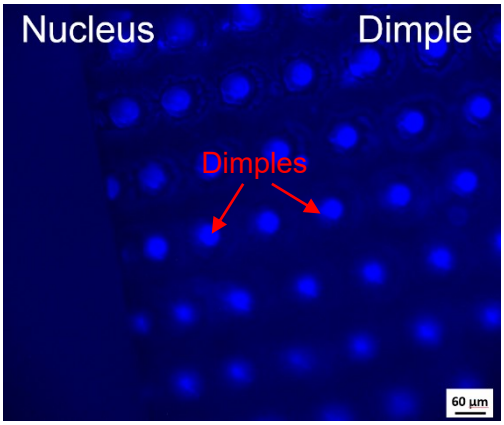

(c)

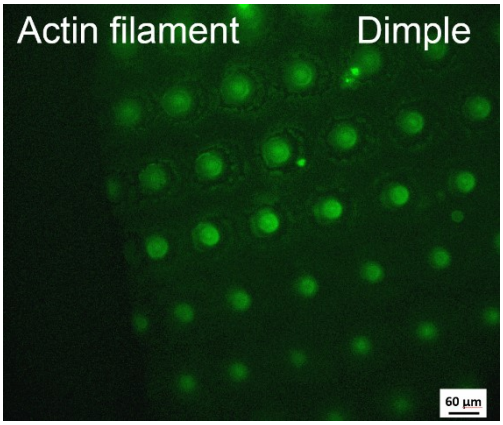

(d)

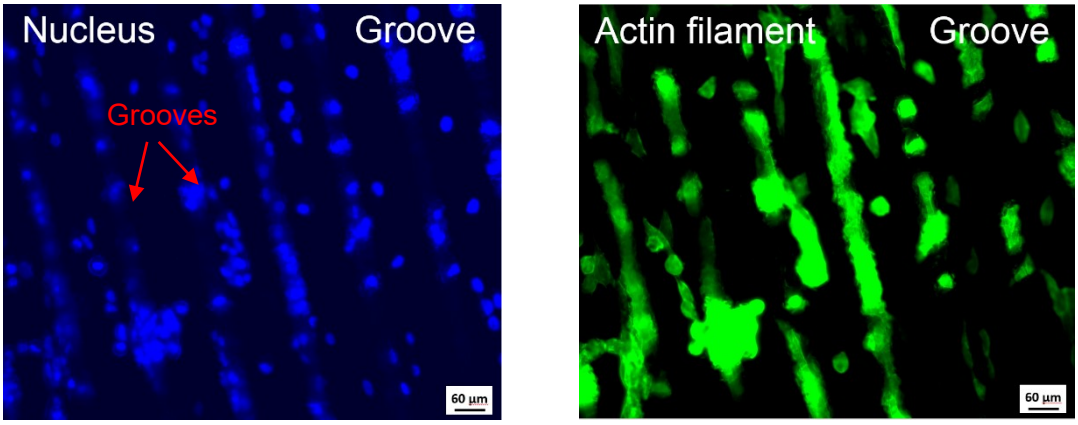

(e) (f)

Fig. 8. Morphologies of MG63 cells cultured on Vitreloy 105 surfaces, namely on the as-cast (a) (b), dimple-textured (c) (d) and groove-textured (e) (f) specimens; (a) (c) (e) cell nucleus stained with DAPI; (b) (d) (f) actin filament stained with phalloidin

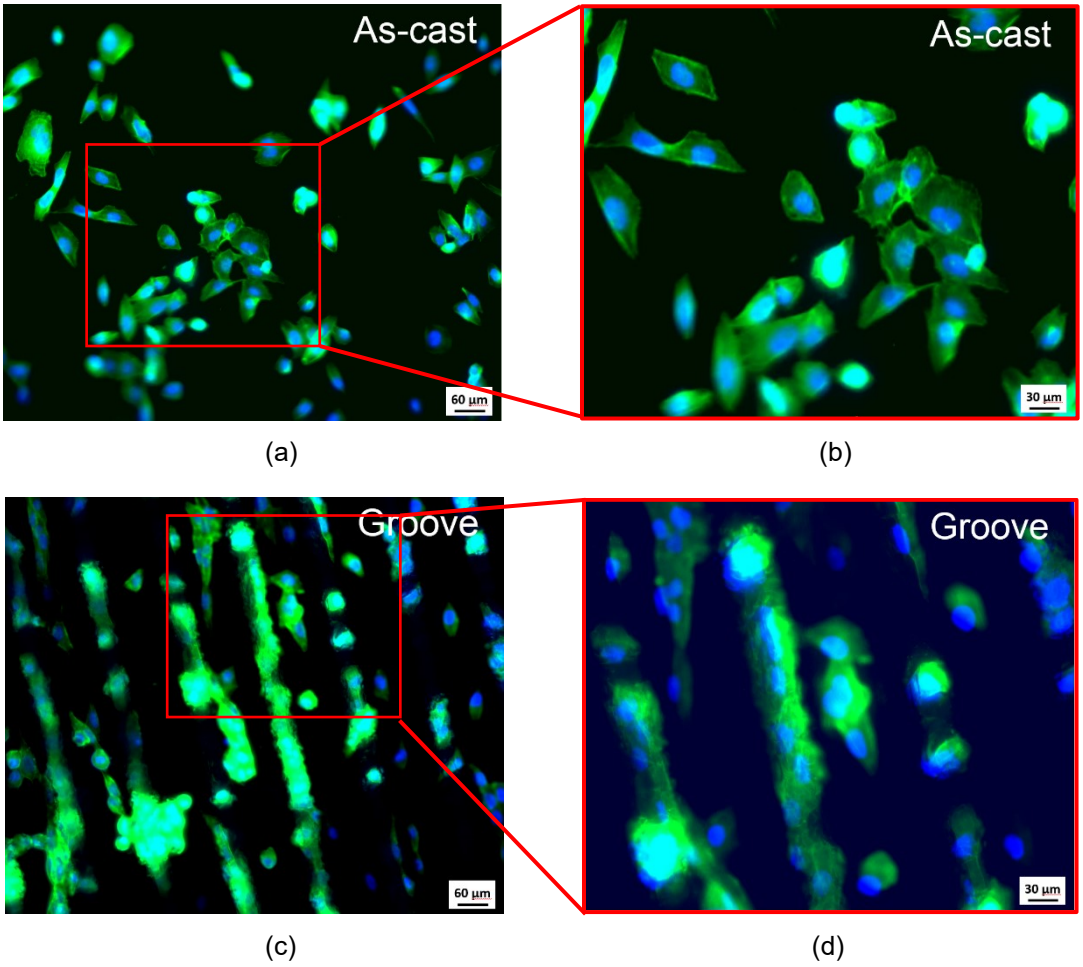

(a) (b)

(c) (d)

Fig. 9 Morphology of the MG63 cells stained with both DAPI and phalloidin; (a) (b) as-cast; (c) (d) groove texture; (b) and (d) are the enlarged view of (a) and (c), respectively.

4. Discussion

4.1 Effects of surface chemical composition

Enhanced cellular attachment and cell viability were clearly observed on the GT surface, as evidenced in Fig. 7 and Fig. 8. It was reported by Ohtsu et al. [36] that enhanced cell adhesion could be attributed to improved surface hydrophilicity. In a previous study from the current authors, the change in hydrophilicity between the three different types of surfaces considered here was shown to result from the combined effects of laser-induced surface roughness and carbon group variations [37]. In addition to the wettability, the chemical composition of the considered specimens could play a negative role in the resulting cytocompatibility, especially the potential toxicity of copper, nickel and aluminium elements [38-40]. The surfaces of the Vitreloy 105 material were found to mainly consist of TiO_2, ZrO_2 and Al_2O_3, as evidenced by the XPS results. These oxides can act as a barrier, avoiding the release of toxic elements from the original metallic glass surface. As a result, such elements may not directly interact with cells, allowing their survival on Vitreloy 105, whether as-cast or laser-irradiated.

4.2 Effect of surface roughness

According to Huang et al. [29], who conducted cellular response experiments on another type of Zr-based BMG, in addition to the chemical composition, the roughness of a surface can also affect cell behaviour. In particular, these authors found that rougher surfaces promoted cell adhesion and proliferation. In the case of laser textured Ti-6Al-4V surfaces, it was reported that the rougher surface provided more features (e.g. redeposited vapour particles and sharp ridges) for the focal adhesions of the cells [41]. In the current study, a higher level of cell attachment (c.f. Fig. 8) was observed for the GT surface, while there were almost no cells attached on the DT sample. Thus, while the relationship between increased roughness and improved cell attachment is observed for the GT sample, it is not verified for the DT specimen. Indeed, the roughness of the DT surface is higher than that of the as-cast sample, but cell attachment was not found to be improved with the dimple pattern. However, it is worth remembering that the hydrophilicity of the original surface was enhanced by the laser-induced groove patterns but weakened by the laser-induced dimple patterns. Thus, it can be said that the cell attachment results show good consistency with the wettability observations and that while surface roughness can affect cell attachment, it is not the only factor determining this aspect of cell behaviour.

Several research investigations have shown that cells align along grooves [35, 41, 42], depending on their dimensions, especially as a function of the depth of the micro-grooves. In particular, it was reported that cells can elongate along, or parallel to, 5 μm deep grooves, but randomly orientate when grooves were only 0.5 μm in depth [35]. In this study, the average depth of the grooves was measured to be about 10 μm. Thus, it is believed that the depth of the grooves generated here was large enough for numerous cells to align preferentially along their lengths. In contrast, the observed randomly aligned cells on the as-cast surface can be attributed to its relatively smooth nature.

4.3 Relationship between cell attachment and wettability

Wettability and surface free energy also contribute to cell attachment [43-46]. In particular, a high surface free energy and increased hydrophilicity can enhance the interaction between an implant surface and its biological environment, cell adhesion and cell spreading [47-49]. In the present study, the measured water contact angles for all samples were smaller than the Berg limit (θ=65°) and thus all surfaces were considered hydrophilic. As reported with Fig. 5, the contact angle of the DT surface was the largest, while that of the groove-textured specimen was the smallest. This means that the dimple pattern resulted in the lowest hydrophilicity while the groove pattern displayed the highest hydrophilicity. In addition, according to Sarapirom et al. [50], the polar component of surface energy has a beneficial effect on enhancing wettability. The results presented earlier showed that the SFE and its polar component for the dimple-textured sample was lower than for the other two types of surfaces considered. Thus, while the dimple-textured surface maintained a hydrophilic nature and displayed a higher surface roughness than that of the as-cast specimen, its reduced wettability post-LST still resulted in decreased cell attachment.

In addition, cell attachment may relate to protein pre-adsorption. It is widely reported that protein adsorption occurs before cells reach the material surface, exposing cell binding domains that may encourage or inhibit cell adhesion [44, 51]. Therefore, the initial surface texture may have implications on protein adsorption, and thus affect cell adhesion. More specifically, fetal bovine serum (FBS), which is the constituent of the cell culture media used in this study, contains proteins such as bovine serum albumin (BSA) and fibronectin which play a role in cell attachment. BSA can partially inhibit osteoblast attachment whilst fibronectin can mediate attachment. It was reported that BSA preferentially adsorbs onto smooth surfaces, whilst fibronectin adsorbs more preferably on rough surfaces [44, 52]. In comparison with the relatively smooth as-cast surface, the rough GT sample surface displayed good cell

attachment, which may be attributed to its greater levels of fibronectin adsorption. Further work investigating the attachment of these serum proteins to these surfaces however is required to test the different roles of BSA and fibronectin. At the same time, the rough dimple-textured surface did not result in good cell attachment. This is likely because protein adsorption can also correlate with surface hydrophilicity and surface free energy [46], highlighting the complex biological process of cell attachment to implant surfaces.

Finally, it should be noted that corrosion resistance is also a characteristic of utmost important for implants due to the aggressive environment encountered *in vivo*. Indeed, corrosion resistance determines the likelihood and rate of released metal ions from implants which can affect cytocompatibility, mechanical properties and failure rates. Therefore, investigations in metal ion release via biocorrosion studies and enhanced corrosion resistance via surface treatment techniques remain a vital issue. Further investigations on the biocorrosion resistance and *in vivo* animal testing are still required to gain a more comprehensive understanding of the cytocompatibility of the laser textured Vitreloy 105 BMG.

5. Conclusions

Two types of surface patterns, dimples and grooves, were fabricated on the surface of the $Zr_{52.8}Cu_{17.6}Ni_{14.8}Al_{9.9}Ti_{4.9}$ BMG, i.e. Vitreloy 105, via laser surface texturing. The resulting cytocompatibility of this glassy alloy pre and post laser processing was investigated and compared using cellular response studies of osteoblast-like cells (MG63) for different conditions, i.e. as-cast, dimple-textured and groove-textured surfaces. The viability of the MG63 cells was evaluated using the CCK-8 assay and comparisons of cell attachment and cell morphology were made via fluorescent image analysis. Surface chemistry, roughness and surface free energy were also assessed and their effects on cytocompatibility discussed in an attempt to explore the underlying laser-induced physical modifications for different patterns. Based on this investigation, the following conclusions can be made:

(1) The Zr-based Vitreloy 105 metallic glass was found to be non-toxic to MG63 osteoblast-like cells. This was attributed to the presence of a surface oxide layer composed of TiO_2, Al_2O_3 and ZrO_2.

(2) Cell viability and attachment could be modified using LST on this type of BMG surface, with the best cytocompatibility achieved when texturing a groove pattern.

(3) Increased presence of metallic oxides and enhanced hydrophilicity of the groove-textured sample are thought to be the main contributors for the improved cytocompatibility.

(4) Cell attachment was significantly decreased for the dimple-textured pattern.

(5) The reduced hydrophilicity resulting from the laser texturing operation for the dimple pattern is likely the driving mechanism for its reduced cytocompatibility.

(6) Cells preferentially orientated along the grooves, whilst attachment direction was random on the as-cast surface.

Acknowledgments

The authors would like to thank Mrs Jiamei Liu from the Instrumental Analysis Center of Xi'an Jiaotong University for her assistance in the XPS measurements; Dr David Waugh from Coventry University for his help in contact angle measurement and Dr Shahin Mehraban from Swansea University for the provision of the DSC data. The lead author (Yang Jiao) gratefully appreciates the financial support from Cardiff University, UK and Xi'an Jiaotong University, China. Emmanuel Brousseau gratefully acknowledges the financial support provided by the Welsh Government and Higher Education Funding Council for Wales through the Sêr Cymru National Research Network in Advanced Engineering and Materials.

References

[1] P. Meagher, E.D. O'Cearbhaill, J.H. Byrne, D.J. Browne, Bulk Metallic Glasses for Implantable Medical Devices and Surgical Tools, Adv Mater 28(27) (2016) 5755-62.

[2] M.D. Demetriou, A. Wiest, D.C. Hofmann, W.L. Johnson, B. Han, N. Wolfson, G. Wang, P.K. Liaw, Amorphous metals for hard-tissue prosthesis, JOM 62(2) (2010) 83-91.

[3] N.H. Tariq, B.A. Hasan, J.I. Akhter, F. Ali, Mechanical and tribological properties of Zr–Al–Ni–Cu bulk metallic glasses, Journal of Alloys and Compounds 469(1-2) (2009) 179-185.

[4] L. Huang, D. Qiao, B.A. Green, P.K. Liaw, J. Wang, S. Pang, T. Zhang, Bio-corrosion study on zirconium-based bulk-metallic glasses, Intermetallics 17(4) (2009) 195-199.

[5] G. Kumar, H.X. Tang, J. Schroers, Nanomoulding with amorphous metals, Nature 457(7231) (2009) 868-72.

[6] V.M. Villapún, B. Qu, P.A. Lund, W. Wei, L. Dover, J.R. Thompson, J.O. Adesina, C. Hoerdemann, S. Cox, S. González, Optimizing the antimicrobial performance of metallic glass composites through surface texturing, Materials Today Communications (2020) 101074.

[7] P. Meagher, E.D. O'Cearbhaill, J.H. Byrne, D.J. Browne, Bulk metallic glasses for implantable medical devices and surgical tools, Advanced Materials 28(27) (2016) 5755-5762.

[8] H.F. Li, Y.F. Zheng, Recent advances in bulk metallic glasses for biomedical applications, Acta Biomater 36 (2016) 1-20.

[9] H.X.T. G. Kumar, J. Schroers, Nanomoulding with amorphous metals, Nature 457 (2009) 868-873.

[10] Y. Liu, Y.-M. Wang, H.-F. Pang, Q. Zhao, L. Liu, A Ni-free ZrCuFeAlAg bulk metallic glass with potential for biomedical applications, Acta biomaterialia 9(6) (2013) 7043-7053.

[11] Y. Yang, K.-H. Kim, J.L. Ong, A review on calcium phosphate coatings produced using a sputtering process—an alternative to plasma spraying, Biomaterials 26(3) (2005) 327-337.

[12] T.R. Rautray, R. Narayanan, K.-H. Kim, Ion implantation of titanium based biomaterials, Progress in Materials Science 56(8) (2011) 1137-1177.

[13] R. Kumari, T. Scharnweber, W. Pfleging, H. Besser, J.D. Majumdar, Laser surface textured titanium alloy (Ti–6Al–4V) – Part II – Studies on bio-compatibility, Applied Surface Science 357 (2015) 750-758.

[14] J. Wahab, M.J. Ghazali, W.M.W. Yusoff, Z. Sajuri, Enhancing material performance through laser surface texturing: A review, Transactions of the IMF 94(4) (2016) 193-198.

[15] W.-T. Hsiao, H.-C. Chang, A. Nanci, R. Durand, Surface microtexturing of Ti–6Al–4V using an ultraviolet laser system, Materials & Design 90 (2016) 891-895.

[16] B.E. Lee, H. Exir, A. Weck, K. Grandfield, Characterization and evaluation of femtosecond laser-induced sub-micron periodic structures generated on titanium to improve osseointegration of implants, Applied Surface Science 441 (2018) 1034-1042.

[17] S. Mukherjee, S. Dhara, P. Saha, Enhancing the cytocompatibility of Ti6Al4V implants by laser surface microtexturing: an in vitro study, The International Journal of Advanced Manufacturing Technology 76(1-4) (2013) 5-15.

[18] N. Ohtsu, T. Kozuka, M. Yamane, H. Arai, Surface chemistry and osteoblast-like cell response on a titanium surface modified by a focused Nd: YAG laser, Surface and Coatings Technology 309 (2017) 220-226.

[19] Z. Yu, G. Yang, W. Zhang, J. Hu, Investigating the effect of picosecond laser texturing on microstructure and biofunctionalization of titanium alloy, Journal of Materials Processing Technology 255 (2018) 129-136.

[20] A. Cunha, A.-M. Elie, L. Plawinski, A.P. Serro, A.M. Botelho do Rego, A. Almeida, M.C. Urdaci, M.-C. Durrieu, R. Vilar, Femtosecond laser surface texturing

of titanium as a method to reduce the adhesion of Staphylococcus aureus and biofilm formation, Applied Surface Science 360 (2016) 485-493.

[21] S.E. Naleway, R.B. Greene, B. Gludovatz, N.K.N. Dave, R.O. Ritchie, J.J. Kruzic, A Highly Fatigue-Resistant Zr-Based Bulk Metallic Glass, Metallurgical and Materials Transactions A 44(13) (2013) 5688-5693.

[22] S.C. Glade, R. Busch, D.S. Lee, W.L. Johnson, R.K. Wunderlich, H.J. Fecht, Thermodynamics of Cu47Ti34Zr11Ni8, Zr52.5Cu17.9Ni14.6Al10Ti5 and Zr57Cu15.4Ni12.6Al10Nb5 bulk metallic glass forming alloys, Journal of Applied Physics 87(10) (2000) 7242-7248.

[23] X.H. Lin, W.L. Johnson, W.K. Rhim, Effect of Oxygen Impurity on Crystallization of an Undercooled Bulk Glass Forming Zr–Ti–Cu–Ni–Al Alloy, Materials Transactions 38 (1997) 473-477.

[24] D.K. Owens, R. Wendt, Estimation of the surface free energy of polymers, Journal of applied polymer science 13(8) (1969) 1741-1747.

[25] Y. Sun, Y. Huang, H. Fan, Y. Wang, Z. Ning, F. Liu, D. Feng, X. Jin, J. Shen, J. Sun, In vitro and in vivo cytocompatibility of an Ag-bearing Zr-based bulk metallic glass for potential medical use, Journal of Non-Crystalline Solids 419 (2015) 82-91.

[26] J. Li, L.-l. Shi, Z.-d. Zhu, Q. He, H.-j. Ai, J. Xu, Zr61Ti2Cu25Al12 metallic glass for potential use in dental implants: Cytocompatibility assessment by in vitro cellular responses, Materials Science and Engineering: C 33(4) (2013) 2113-2121.

[27] J. Li, H.-j. Ai, The responses of endothelial cells to Zr61Ti2Cu25Al12 metallic glass in vitro and in vivo, Materials Science and Engineering: C 40 (2014) 189-196.

[28] Y. Jiao, E. Brousseau, Q. Han, H. Zhu, S. Bigot, Investigations in nanosecond laser micromachining on the Zr52. 8Cu17. 6Ni14. 8Al9. 9Ti4. 9 bulk metallic glass: experimental and theoretical study, Journal of Materials Processing Technology 273 (2019) 116232.

[29] L. Huang, Z. Cao, H. Meyer, P. Liaw, E. Garlea, J. Dunlap, T. Zhang, W. He, Responses of bone-forming cells on pre-immersed Zr-based bulk metallic glasses: Effects of composition and roughness, Acta biomaterialia 7(1) (2011) 395-405.

[30] W. Pfleging, R. Kumari, H. Besser, T. Scharnweber, J.D. Majumdar, Laser surface textured titanium alloy (Ti–6Al–4V): Part 1 – Surface characterization, Applied Surface Science 355 (2015) 104-111.

[31] P. Bizi-Bandoki, S. Valette, E. Audouard, S. Benayoun, Time dependency of the hydrophilicity and hydrophobicity of metallic alloys subjected to femtosecond laser irradiations, Applied Surface Science 273 (2013) 399-407.

[32] H. Costa, I. Hutchings, Hydrodynamic lubrication of textured steel surfaces under reciprocating sliding conditions, Tribology International 40(8) (2007) 1227-1238.

[33] R. Junker, A. Dimakis, M. Thoneick, J.A. Jansen, Effects of implant surface coatings and composition on bone integration: a systematic review, Clinical oral implants research 20 (2009) 185-206.

[34] O. Raimbault, S. Benayoun, K. Anselme, C. Mauclair, T. Bourgade, A.M. Kietzig, P.L. Girard-Lauriault, S. Valette, C. Donnet, The effects of femtosecond laser-textured Ti-6Al-4V on wettability and cell response, Mater Sci Eng C Mater Biol Appl 69 (2016) 311-20.

[35] K. Anselme, M. Bigerelle, B. Noel, A. Iost, P. Hardouin, Effect of grooved titanium substratum on human osteoblastic cell growth, Journal of Biomedical Materials Research: An Official Journal of The Society for Biomaterials, The Japanese Society for Biomaterials, and The Australian Society for Biomaterials and the Korean Society for Biomaterials 60(4) (2002) 529-540.

[36] N. Ohtsu, T. Kozuka, M. Hirano, H. Arai, Electrolyte effects on the surface chemistry and cellular response of anodized titanium, Applied Surface Science 349 (2015) 911-915.

[37] Y. Jiao, E. Brousseau, X. Shen, X. Wang, Q. Han, H. Zhu, S. Bigot, W. He, Investigations in the fabrication of surface patterns for wettability modification on a Zr-based bulk metallic glass by nanosecond laser surface texturing, Journal of Materials Processing Technology 283 (2020) 116714.

[38] H.-H. Huang, Y.-S. Sun, C.-P. Wu, C.-F. Liu, P.K. Liaw, W. Kai, Corrosion resistance and cytocompatibility of Ni-free Zr-based bulk metallic glass for biomedical applications, Intermetallics 30 (2012) 139-143.

[39] J.Y. Wang, B.H. Wicklund, R.B. Gustilo, D.T. Tsukayama, Prosthetic metals interfere with the functions of human osteoblast cells in vitro, Clinical Orthopaedics and Related Research® 339 (1997) 216-226.

[40] T. Rae, The biological response to titanium and titanium-aluminium-vanadium alloy particles: I. Tissue culture studies, Biomaterials 7(1) (1986) 30-36.

[41] J. Chen, J. Ulerich, E. Abelev, A. Fasasi, C.B. Arnold, W. Soboyejo, An investigation of the initial attachment and orientation of osteoblast-like cells on laser grooved Ti-6Al-4V surfaces, Materials Science and Engineering: C 29(4) (2009) 1442-1452.

[42] K. Chesmel, C. Clark, C. Brighton, J. Black, Cellular responses to chemical and morphologic aspects of biomaterial surfaces. II. The biosynthetic and migratory response of bone cell populations, Journal of biomedical materials research 29(9) (1995) 1101-1110.

[43] L. Ponsonnet, K. Reybier, N. Jaffrezic, V. Comte, C. Lagneau, M. Lissac, C. Martelet, Relationship between surface properties (roughness, wettability) of titanium and titanium alloys and cell behaviour, Materials Science and Engineering: C 23(4) (2003) 551-560.

[44] B.D. Boyan, T.W. Hummert, D.D. Dean, Z. Schwartz, Role of material surfaces in regulating bone and cartilage cell response, Biomaterials 17(2) (1996) 137-146.

[45] W. Chrzanowski, E.A.A. Neel, D.A. Armitage, J.C. Knowles, Effect of surface treatment on the bioactivity of nickel–titanium, Acta Biomaterialia 4(6) (2008) 1969-1984.

[46] A. Ochsenbein, F. Chai, S. Winter, M. Traisnel, J. Breme, H.F. Hildebrand, Osteoblast responses to different oxide coatings produced by the sol–gel process on titanium substrates, Acta biomaterialia 4(5) (2008) 1506-1517.

[47] F. Schwarz, M. Wieland, Z. Schwartz, G. Zhao, F. Rupp, J. Geis‐Gerstorfer, A. Schedle, N. Broggini, M.M. Bornstein, D. Buser, Potential of chemically modified hydrophilic surface characteristics to support tissue integration of titanium dental implants, Journal of Biomedical Materials Research Part B: Applied Biomaterials: An Official Journal of The Society for Biomaterials, The Japanese Society for Biomaterials, and The Australian Society for Biomaterials and the Korean Society for Biomaterials 88(2) (2009) 544-557.

[48] M.E. Schrader, On adhesion of biological substances to low energy solid surfaces, J. Colloid Interface Sci. 88 (1981) 296-297.

[49] R. Baier, A. Meyer, J. Natiella, R. Natiella, J. Carter, Surface properties determine bioadhesive outcomes: methods and results, Journal of biomedical materials research 18(4) (1984) 337-355.

[50] S. Sarapirom, J. Lee, S. Jin, D. Song, L. Yu, J. Han, C. Chaiwong, Wettability effect of PECVD-SiOx films on poly (lactic acid) induced by oxygen plasma on protein adsorption and cell attachment, Journal of Physics: Conference Series, IOP Publishing, 2013, p. 012042.

[51] B.D. Ratner, A.S. Hoffman, F.J. Schoen, J.E. Lemons, Biomaterials science: an introduction to materials in medicine, Elsevier2004.

[52] Y. Yang, R. Cavin, J.L. Ong, Protein adsorption on titanium surfaces and their effect on osteoblast attachment, Journal of Biomedical Materials Research Part A: An Official Journal of The Society for Biomaterials, The Japanese Society for Biomaterials, and The Australian Society for Biomaterials and the Korean Society for Biomaterials 67(1) (2003) 344-349.